

Modulated Spin Dynamics of [Co₂] Coordination Helicates via Differential Strand Composition

Leoní A. Barrios,^{*,a} Nuria Capó,^a Hanae Boulehjour,^c Daniel Reta,^{b,c,d} Inés Tejedor,^e Olivier Roubeau^{*,e} and Guillem Aromí^{*,a}

^a Departament de Química Inorgànica i Orgànica and IN2UB, Universitat de Barcelona, Diagonal 645, 08028 Barcelona, Spain. E-mail: aromi@ub.edu3

^b Faculty of Chemistry, The University of the Basque Country UPV/EHU, Donostia, 20018, Spain

^c Donostia International Physics Center (DIPC), Donostia, 20018, Spain

^d IKERBASQUE, Basque Foundation for Science, Bilbao, 48013, Spain

^e Instituto de Nanociencia y Materiales de Aragón (INMA), CSIC – Universidad de Zaragoza, Plaza San Francisco s/n, 50009, Zaragoza, Spain. E-mail: roubeau@unizar.es

SUPPORTING INFORMATION

Table of contents

Synthetic details	p. S3
Physical characterization	p. S4
Table S1. Crystallographic and refinement details for the structures of 2 and 3	p. S6
Table S2. Details of hydrogen bonds involving the guest anions in structures of 1-3	p. S7
Table S3. Co(II) ions coordination environment in the structures of 1-3	p. S8
Figure S1. ORTEP representation of the supramolecular cation of 1	p. S9
Figure S2. ORTEP representation of the supramolecular cation of 2	p. S10
Figure S3. Supramolecular $\pi \cdots \pi$ interactions in the structure of 2	p. S11
Figure S4. ORTEP representation of the supramolecular cation of 3	p. S12
Figure S5. Supramolecular C–H \cdots π and $\pi \cdots \pi$ interactions in the structure of 3	p. S13
Figure S6. χT vs. T and isothermal magnetization vs. field plots for 1-3	p. S14
Figure S7. χT vs. T and isothermal magnetization vs. field plots per Co for 1 and 3	p. S14
Details of CASSCF calculation procedure	p. S15
Table S4. Energies (CAS(7,5) level) of spin-only and spin-orbit coupled states of 1	p. S17
Table S5. Energies (CAS(7,5) level) of spin-only and spin-orbit coupled states of 2	p. S18
Table S6. Energies (CAS(7,5) level) of spin-only and spin-orbit coupled states of 3	p. S19
Table S7. Energies (CAS(7,5) level), larger basis for 1^a	p. S20
Table S8. Energies (CAS(7,10) level) for 1^a	p. S21
Table S9. Dipolar interaction components calculated for the ground Kramers of 1	p. S22
Table S10. Dipolar interaction components calculated for the ground Kramers of 2	p. S22
Table S11. Dipolar interaction components calculated for the ground Kramers of 3	p. S22
Figure S5. Semi-log experimental and CASSCF-SO χT vs. T for compounds 1 , 2 and 3	p. S23
Figure S6. Frequency dependence of ac magnetic susceptibility of 2 and 3 at 2 K and increasing applied dc fields	p. S24
Figure S7. Low frequency dependence of the ac magnetic susceptibility of 1-3 at 2 K and increasing fields	p. S25

Figure S8. Field dependence of the magnetization relaxation rates of compounds 1-4	p. S26
Figure S9. Frequency dependence of the <i>ac</i> magnetic susceptibility of 2 and 3 at 0.03 T and increasing temperatures	p. S27
Figure S10. Frequency dependence of the <i>ac</i> magnetic susceptibility of 2 and 3 at 0.1 T and increasing temperatures	p. S28
Figure S11. Temperature dependence of the relaxation rates of 2 and 3 at 0.03 T	p. S29
Figure S12. Temperature dependence of the relaxation rates of compounds 1 , 2 , 3 and 4 under a 0.1 T applied field, showing phonon-bottlenecked direct and Raman processes	p. S30
Figure S13. T^n dependence of the magnetization relaxation rates of 1-4 at 0.1 T	p. S31
Table S12. Best-fit parameters for the field dependence of τ^{-1} of 1-4	p. S32
Table S13. Best-fit parameters for the temperature dependence of τ^{-1} of 1-4	p. S33
Figure S14. SEM images showing grain size distribution of the used samples of 1-3	p. S34
Figure S15. Specific heat of 1-3 in zero-field with calculated Debye heat capacity	p. S35

Synthetic details.

Ligand L1 was prepared as previously published.¹ Compounds **1** and **4** were obtained according to our previous published procedures.² Ligand L2 was prepared following the published protocol.³ The rest of the reagents were obtained from commercial sources and used as received.

Cl@[Co₂(L1)₃]Cl(PF₆)₂ (1). This complex was prepared as previously published by us.²

SiF₆@[Co₂(L1)₂(L2)](PF₆)₂ (2). A suspension of L1 (7.8 mg, 0.021 mmol) and L2 (20 mg, 0.042 mmol) in 10 mL of methanol was added dropwise to a 5 mL of methanolic solution of Co(BF₄)₂·6H₂O (14.6 mg, 0.042 mmol). The mixture was stirred for 30 min while a change of color from light red to yellow was observed while the solution turned cloudy. The solution was then filtered with a nylon membrane (0.2 μm pore size), yielding a yellow filtrate to which a solution of Bu₄NPF₆ (33.2 mg, 0.086 mmol) in 5 mL of methanol was then added dropwise. After stirring for 10 min, mixture was filtered again with a membrane with 0.2 μm pores and the resulting filtrate was layered in toluene. Orange crystals were obtained after 10 days. Yield(%): 41%. IR: 3151 (s N-H), 1623 (b -N-H), 1566 (s C=C), 1438 (s C=C), 837 (s P-F), 781 (s Si-F), 697 (s Si-F) cm⁻¹. Anal. Calc. (Found) for 2·CH₃OH·0.55C₇H₈: C, 53.93 (53.92); H, 3.77 (3.68); N, 13.04 (12.94).

ClO₄@[Co₂(L2)₃](ClO₄)₃ (3). Dropwise addition of a 5 mL methanolic light red solution of Co(ClO₄)₂·6H₂O (10 mg, 0.027 mmol) to a suspension of L2 (20 mg, 0.043 mmol) in methanol (10 mL) led to a cloudy light yellow suspension after stirring for 30 min. The suspension was then filtered with a nylon membrane of 0.2 μm pore size and a solution of Bu₄NClO₄ (19.4 mg, 0.056 mmol) in 5 mL of methanol was added dropwise to the resulting filtrate. Then, the mixture was left stirring for 10 min and filtered again with a membrane with 0.2 μm pores. The crystallization was carried out by vapor diffusion of diethyl ether. After 2 weeks, yellow crystals were obtained. Yield(%): 26%. IR: 2363 (s C-H), 1622 (b -N-H), 1557 (s C=C), 1435 (s C=C), 1083 (s Cl-O), 796 (b C-H) cm⁻¹. Anal. Calc. (Found) for 3·H₂O:C, 52.66 (52.23); H, 4.25 (3.81); N, 12.28 (11.92).

¹ M. Darawsheh, L. A. Barrios, O. Roubeau, S. J. Teat, G. Aromí, *Chem., Eur. J.* **2016**, *22*, 8635-8645.

² R. Diego, A. Pavlov, M. Darawsheh, D. Aleshin, J. Nehr Korn, Y. Nelyubina, O. Roubeau, V. Novikov, G. Aromí, *Inorg. Chem.* **2019**, *58*, 9562-9566.

³ M. Darawsheh, L. A. Barrios, O. Roubeau, S. J. Teat, G. Aromí, *Angew. Chem., Int. Ed.* **2018**, *57*, 13509-13513.

Physical characterization

Single Crystal X-ray Diffraction (SCXRD).

Data for compound **2** were obtained at 100 K on an orange rod of dimensions 0.133 x 0.048 x 0.012 mm³ at Beamline 12.2.1 of the Advanced Light Source (Berkeley, USA), on a Bruker D8 diffractometer equipped with a PHOTON II detector and using silicon (111) monochromated synchrotron radiation ($\lambda = 0.7288 \text{ \AA}$). Data for compound **3** were obtained at 100 K on an orange rod of dimensions 0.145 x 0.045 x 0.032 mm³ using a Bruker Smart APEX diffractometer. Data reduction and absorption corrections were performed with SAINT and SADABS, respectively.⁴ The structures were solved by intrinsic phasing with SHELXT⁵ and refined by full-matrix least-squares on F² with SHELXL.⁶ The structure of **2** was refined as a 2-component inversion twin.

All details can be found in CCDC 2304058 (**2**) and 2304059 (**3**) that contain the supplementary crystallographic data for this paper. These data can be obtained free of charge from The Cambridge Crystallographic Data Center via <https://summary.ccdc.cam.ac.uk/structure-summary-form>. Crystallographic and refinement parameters are summarized in Table S1. Details of hydrogen bonds involving the guest anions and of the coordination environment of the Co(II) ions are given in Tables S2 and S3 respectively.

Scanning Electron Microscopy

Observations were made through the Laboratorio de Microscopías Avanzadas (LMA) with an FEI INSPECT-F50 microscope working at 10 kV. Samples were coated with a conductive layer of Pd. Analysis of images was done with Digital Micrograph software.

Magnetic properties.

Direct current (*dc*) measurements were performed with a commercial MPMS-XL SQUID magnetometer hosted by the Physical Measurements Unit of the Servicio General de Apoyo a la Investigación-SAI, Universidad de Zaragoza. The data were corrected for the contribution of the capsule sample holder, determined empirically. The sample diamagnetic contributions to the susceptibility were corrected using Pascal's constant tables.

Isothermal alternating current (*ac*) measurements were collected with the ACMS option of a commercial PPMS set-up with a 4 Oe field oscillating in the range $10 \leq \nu \leq 10000 \text{ Hz}$. Measurements were performed at 2 K at various applied *dc* fields in the range 0-15000 Oe, and then at 300 and 1000 Oe at various temperatures up to 10 K. Because a low frequency tail appearing at high fields and 2 K seemed to indicate the presence of a slower relaxation mode, further measurements in the range $0.03 \leq \nu \leq 100 \text{ Hz}$ were performed with the same 4 Oe amplitude at 2 K and fields from 3000 to 15000 Oe using the MPMS-XL SQUID magnetometer. In all magnetic measurements, the samples were in the form of polycrystalline powders, either as obtained or lightly crushed in cases like compound **1** where relatively large crystallites were present. Overall, all samples had crystallite size in the 1-10 μm range (see Fig. S15), *a priori* precluding the presence of significant size/shape phonon bottleneck.

The characteristic relaxation times τ were extracted from the frequency dependence of the real and imaginary components of the *ac* susceptibility χ' and χ'' using the following expressions corresponding to the generalized Debye model:

⁴ G. M. Sheldrick, 2012, *SAINT and SADABS*, Bruker AXS Inc., Madison, Wisconsin, USA.

⁵ G. M. Sheldrick, *Acta Cryst. A*, 2015, **71**, 3-8

⁶ G. M. Sheldrick, *Acta Cryst. C*, 2015, **71**, 3-8

$$\chi'(\omega) = \chi_S + (\chi_T - \chi_S) \frac{1 + (\omega\tau)^\beta \cos\left(\frac{\pi\beta}{2}\right)}{1 + 2(\omega\tau)^\beta \cos\left(\frac{\pi\beta}{2}\right) + (\omega\tau)^{2\beta}}$$

$$\chi''(\omega) = (\chi_T - \chi_S) \frac{(\omega\tau)^\beta \sin\left(\frac{\pi\beta}{2}\right)}{1 + 2(\omega\tau)^\beta \cos\left(\frac{\pi\beta}{2}\right) + (\omega\tau)^{2\beta}}$$

in which ω is the angular frequency, χ_T the isothermal susceptibility, χ_S the adiabatic susceptibility and β describes the distribution of relaxation times. β was found to be close to 1 in the case of **1** and **4** (0.88-1 range), indicating a limited distribution of relaxation times. In the case of **2** and **3**, correct simulation of the width of the peak in the experimental χ'' vs. frequency data requires in all cases β in the range 1-1.25, which has no physical meaning. β was therefore fixed to 1, resulting in relatively poorer fits, albeit with no significant effect on the estimation of the relaxation rates.

Heat capacity

Heat capacities in the range of 0.35–100 K were obtained using the relaxation method in a commercial ^3He set-up equipped with a 9 T magnet, at the Physical Measurements Unit of the Servicio General de Apoyo a la Investigación-SAI, Universidad de Zaragoza. Apiezon-N grease was used to provide good internal thermal contact between the heater, thermometer and sample. The samples were in the form of thin pellets.

Differential Scanning Calorimetry (DSC) was used to obtain heat capacity in the range 100-300 K. Measurements were done with a Q1000 calorimeter from TA Instruments equipped with the LNCS accessory. Calibration of the temperature and enthalpy scales was achieved with a standard sample of In, using its melting transition (156.6 °C, 3296 Jmol⁻¹). Mechanically crimped Al pans with an empty pan as a reference were used. Data were obtained at a scanning rate of 10 Kmin⁻¹. Measurements of a sapphire reference sample under the same conditions were used to correct the obtained values of heat capacity.

Considering that the low temperature components in Figure 6 would arise from weak spin-spin interactions, the corresponding average dipolar magnetic field $\langle B_{dip} \rangle$ seen by each Co(II) ion was estimated through a high temperature series for dipolar interactions using the expression⁷

$$\frac{C_{dip}}{R} \approx \frac{\mu_{eff}^2 \langle B_{dip} \rangle^2}{2(k_B T)^2}$$

Using the experimental magnetic susceptibility data at 2 K to define μ_{eff} , the $\langle B_{dip} \rangle$ that best represent the low temperature heat capacity tail are estimated as ca. 6, 24 and 28 mT respectively for **1**, **2** and **3**.

⁷ S. Gómez-Coca, A. Urtizbera, E. Cremades, P. J. Alonso, A. Camón, E. Ruiz, F. Luis, *Nature Commun.*, **2014**, 5:4300

Table S1. Crystallographic and refinement parameters for the structures of compounds **2** and **3**.

	2	3
Formula	C ₈₂ H ₆₄ Co ₂ N ₁₈ , 2(PF ₆), SiF ₆ , 0.415(C ₇ H ₈), 3.756(CH ₄ O)	C ₉₀ H ₇₂ Co ₂ N ₁₈ , 4(ClO ₄), 0.5(C ₄ H ₁₀ O), 9(CH ₄ O), 2(H ₂ O)
FW (g mol ⁻¹)	2009.95	2282.78
<i>T</i> (K)	100	100
Wavelength (Å)	0.7288	0.71073
Crystal system	monoclinic	monoclinic
Space group	Cc	<i>P</i> 2 ₁ / <i>n</i>
<i>a</i> (Å)	22.5655(10)	22.9697(11)
<i>b</i> (Å)	26.8138(10)	18.0372(10)
<i>c</i> (Å)	17.7992(7)	27.1574(12)
α (°)	90	90
β (°)	125.705(3)	94.966(2)
γ (°)	90	90
<i>V</i> (Å ³)	8745.3(7)	11209.3(10)
<i>Z</i>	4	4
ρ_{calcd} (g cm ⁻³)	1.527	1.352
μ (mm ⁻¹)	0.565	0.474
Independent reflections (<i>R</i> _{int})	21947 (0.0300)	15564 (0.0722)
parameters / restraints	1269 / 250	1508 / 429
Flack parameter	0.506(11)	-
Goodness-of-fit	1.037	1.038
Final <i>R</i> 1 / <i>wR</i> 2 [<i>I</i> > 2 σ (<i>I</i>)]	0.0450 / 0.1251	0.0935 / 0.2502
Final <i>R</i> 1 / <i>wR</i> 2 [all data]	0.0482 / 0.1281	0.1324 / 0.2801
largest diff. peak / hole (e Å ³)	1.194 / -0.883	1.920 / -1.119

Table S2. Hydrogen bonds involving the guest anion in the structures of compounds **1**,⁸ **2**, and **3**.

	D–H⋯A	D–H (Å)	H⋯A (Å)	D⋯A (Å)	D–H⋯A (°)
1	N3–H3B⋯Cl1 ^a	0.88	3.16	3.555(9)	110.1
	N4–H4B⋯Cl1 ^a	0.88	3.46	2.779(10)	152.3
	N9–H9A⋯Cl1	0.88	2.49	3.257(6)	145.8
	N10–H10B⋯Cl1 ^a	0.88	3.11	3.637(8)	120.4
	N15–H15A⋯Cl1	0.88	2.38	3.136(6)	144.1
	N16–H16B⋯Cl1 ^a	0.88	2.73	3.418(6)	135.4
2	N3–H3A⋯F3	0.88	1.99	2.835(4)	159.9
	N4–H4B⋯F6	0.88	1.93	2.750(4)	154.2
	N9–H9A⋯F4	0.88	1.91	2.720(4)	152.1
	N10–H10B⋯F2	0.88	2.15	2.955(4)	151.2
	N15–H15A⋯F1	0.88	1.83	2.665(4)	157.9
	N16–H16B⋯F5	0.88	1.79	2.622(4)	156.4
3	N3–H3A⋯O1 ^a	0.88	2.81	3.130(10)	102.8
	N4–H4B⋯O2 ^a	0.88	3.40	3.804(10)	111.2
	N9–H9A⋯O1	0.88	2.19	2.845(10)	130.9
	N10–H10B⋯O4 ^a	0.88	3.27	3.675(10)	110.5
	N15–H15A⋯O1 ^a	0.88	3.01	3.401(10)	108.8
	N16–H16B⋯O3 ^a	0.88	3.52	3.997(10)	116.7

^a Note that these hydrogens form a stronger hydrogen bond with acceptors from lattice solvent molecules (or the outer Cl counterion in the case of **1**)

⁸ R. Diego, A. Pavlov, M. Darawsheh, D. Aleshin, J. Nehr Korn, Y. Nelyubina, O. Roubeau, V. Novikov and G. Aromí, *Inorg. Chem.* 2019, **58**, 9562-9566

Table S3. Bond lengths (Å) and angles (°) describing the coordination environment of the Co(II) ions in the structures of compounds **1**,⁷ **2** and **3**.

1			
Co1–N14	2.099(6)	Co2–N11	2.099(6)
Co1–N8	2.100(7)	Co2–N5	2.104(6)
Co1–N2	2.106(6)	Co2–N17	2.119(7)
Co1–N7	2.141(6)	Co2–N18	2.128(6)
Co1–N13	2.204(6)	Co2–N6	2.173(6)
Co1–N1	2.213(6)	Co2–N12	2.180(6)
N14–Co1–N7	157.7(2)	N11–Co2–N18	162.8(2)
N2–Co1–N13	161.0(2)	N17–Co2–N6	167.7(2)
N8–Co1–N1	166.3(2)	N5–Co2–N12	167.9(2)
2			
Co1–N8	2.108(3)	Co2–N5	2.090(3)
Co1–N14	2.115(3)	Co2–N17	2.114(3)
Co1–N2	2.134(3)	Co2–N11	2.123(3)
Co1–N13	2.154(3)	Co2–N18	2.129(3)
Co1–N1	2.166(3)	Co2–N6	2.148(3)
Co1–N7	2.171(3)	Co2–N12	2.172(3)
N8–Co1–N1	161.86(13)	N5–Co2–N12	159.85(13)
N2–Co1–N13	164.50(12)	N11–Co2–N18	165.47(12)
N14–Co1–N7	166.92(13)	N17–Co2–N6	169.13(12)
3			
Co1–N14	2.078(5)	Co2–N12B / N12	2.047(19) / 2.223(15)
Co1–N8	2.124(6)	Co2–N17	2.090(6)
Co1–N2	2.124(6)	Co2–N11	2.094(6)
Co1–N7	2.133(6)	Co2–N5	2.107(6)
Co1–N13	2.149(6)	Co2–N6	2.138(6)
Co1–N1	2.169(6)	Co2–N18	2.149(6)
N2–Co1–N7	165.6(2)	N11–Co2–N6	168.7(3)
N8–Co1–N13	169.1(2)	N12 / N12B–Co2–N17	171.8(8) / 172.1(15)
N14–Co1–N1	172.4(2)	N5–Co2–N18	172.1(2)

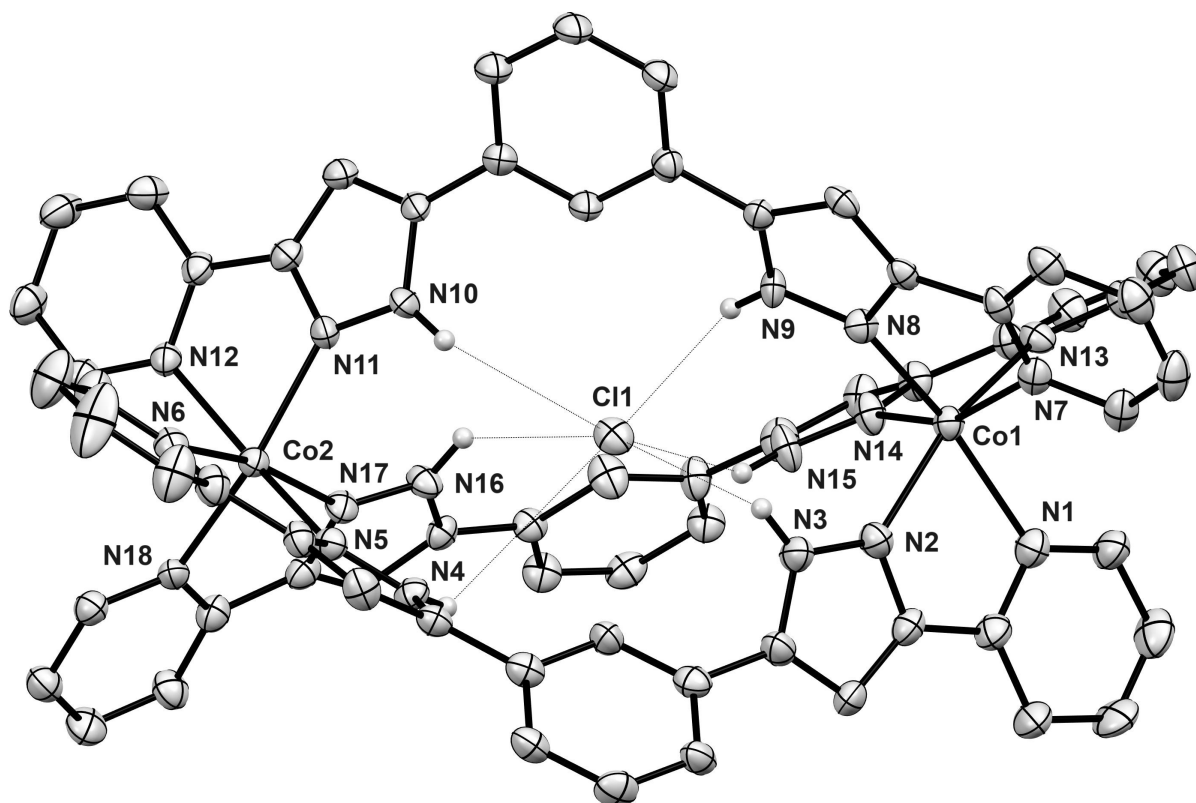


Figure S1. ORTEP representation of the supramolecular cation $\text{Cl}@[Co_2(L1)_3]^{3+}$ of **1** with hetero atoms labelled. Only H from N–H groups are shown. Hydrogen bonds are shown as red dotted lines.

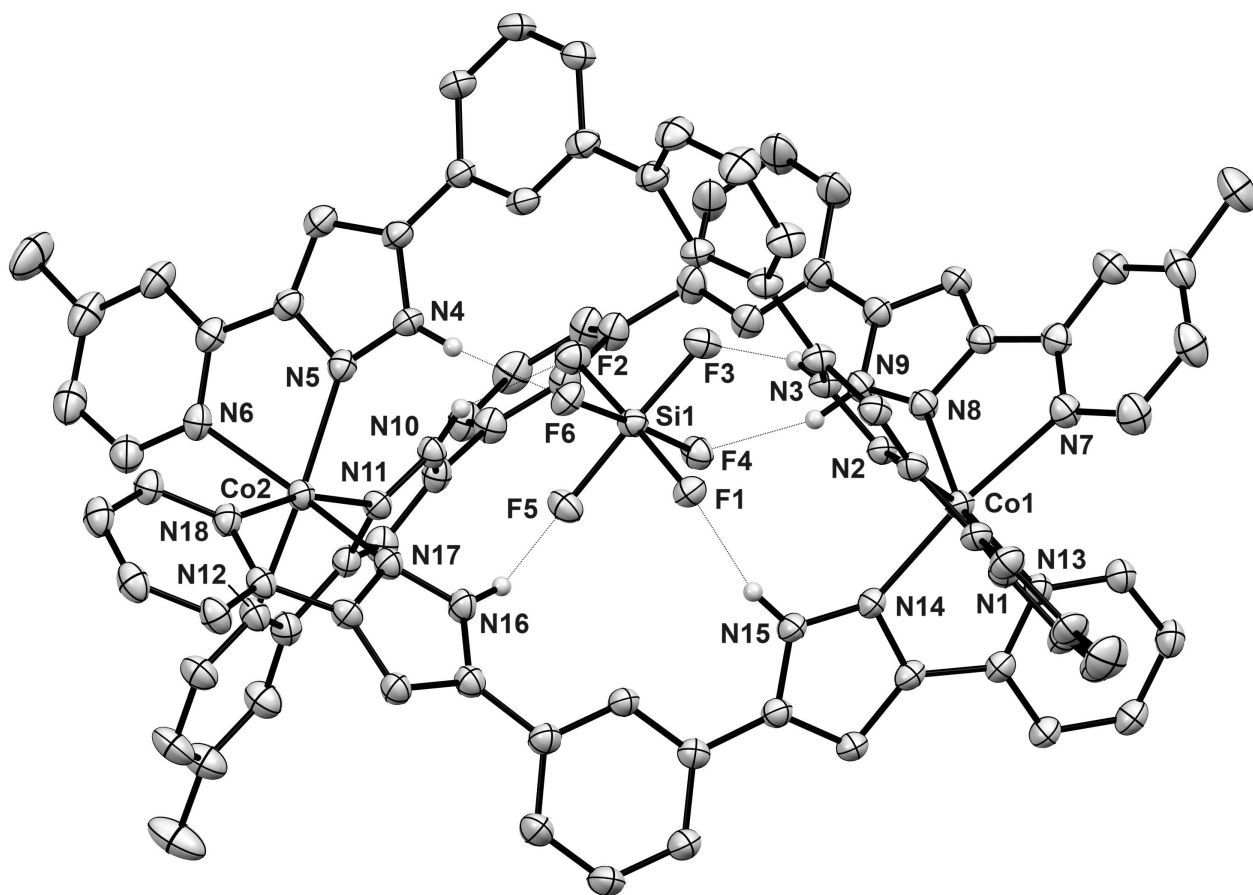


Figure S2. ORTEP representation of the supramolecular $\text{SiF}_6@[\text{Co}_2(\text{L}1)_2(\text{L}2)]^{2+}$ of **2** with hetero atoms labelled. Only H from N–H groups are shown. Hydrogen bonds are shown as red dotted lines.

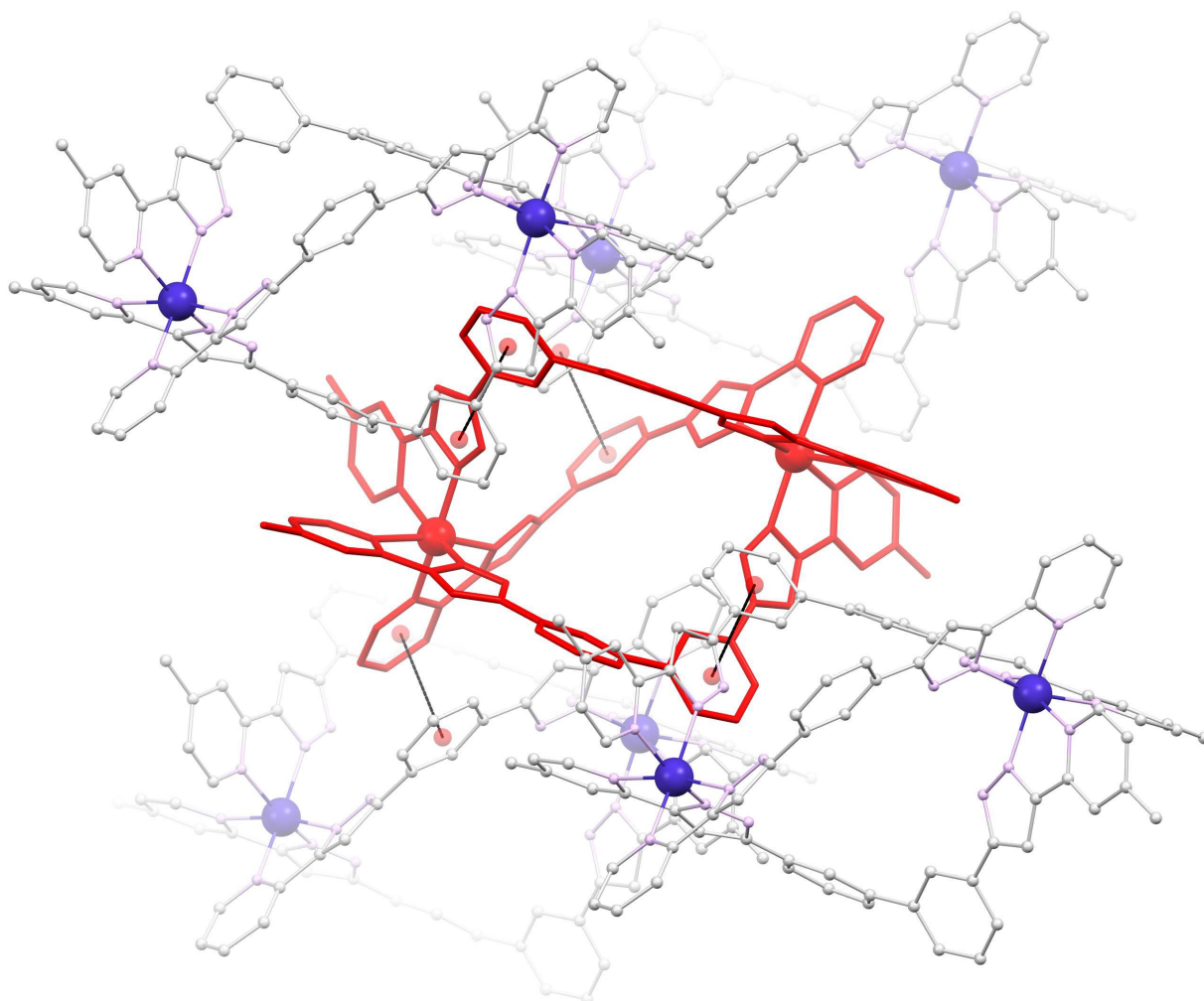


Figure S3. Representation of one $(\text{SiF}_6@[\text{Co}_2(\text{L1})_2(\text{L2})])^{2+}$ unit from **2** (red) together with its four first neighbors in the crystal lattice (the latter with blue, purple and grey balls representing Co, N and C respectively). The interactions with these neighbors are $\pi \cdots \pi$ interactions emphasized by contacts between the centroids (red balls linked by dashed black lines) of the aromatic rings involved. H atoms not shown for clarity.

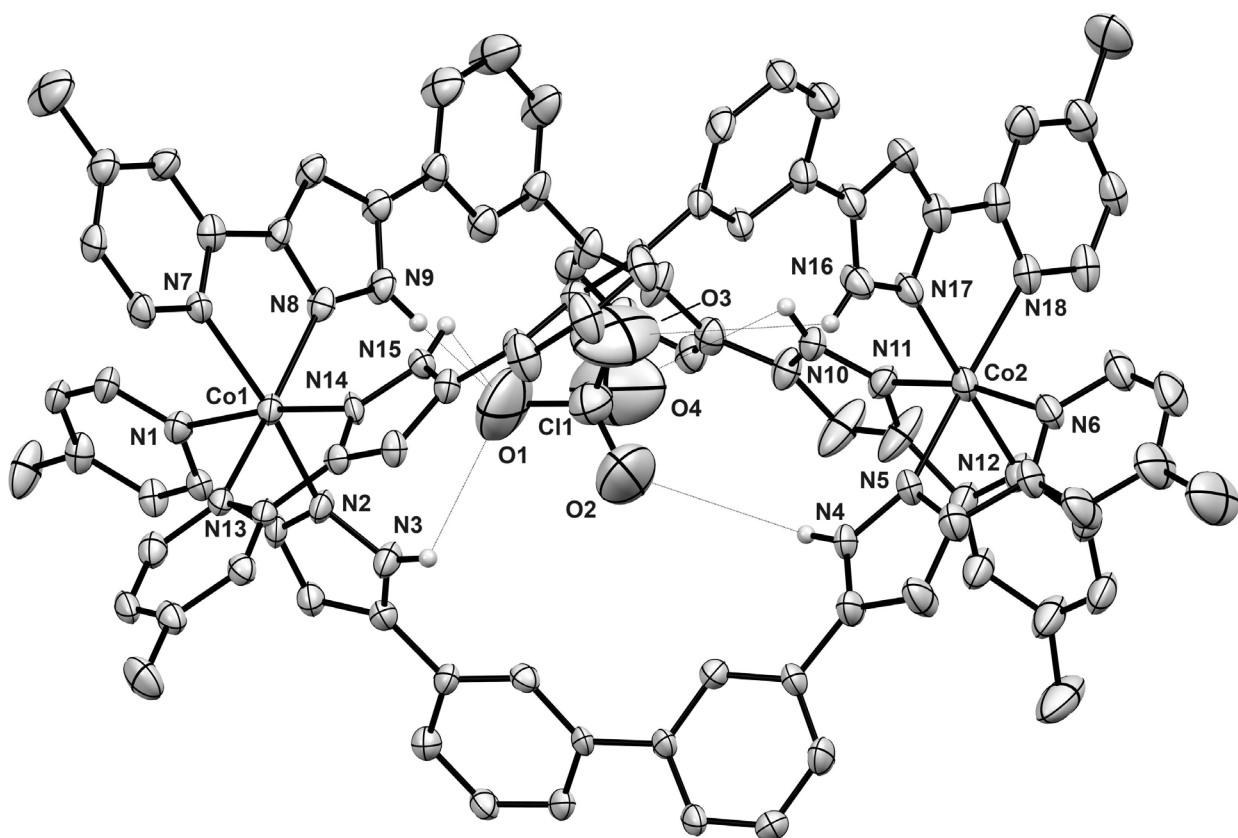


Figure S4. ORTEP representation of the supramolecular $\text{SiF}_6@[\text{Co}_2(\text{L}1)_2(\text{L}2)]^{2+}$ of **2** with hetero atoms labelled. Only H from N–H groups are shown. Hydrogen bonds are shown as red dotted lines.

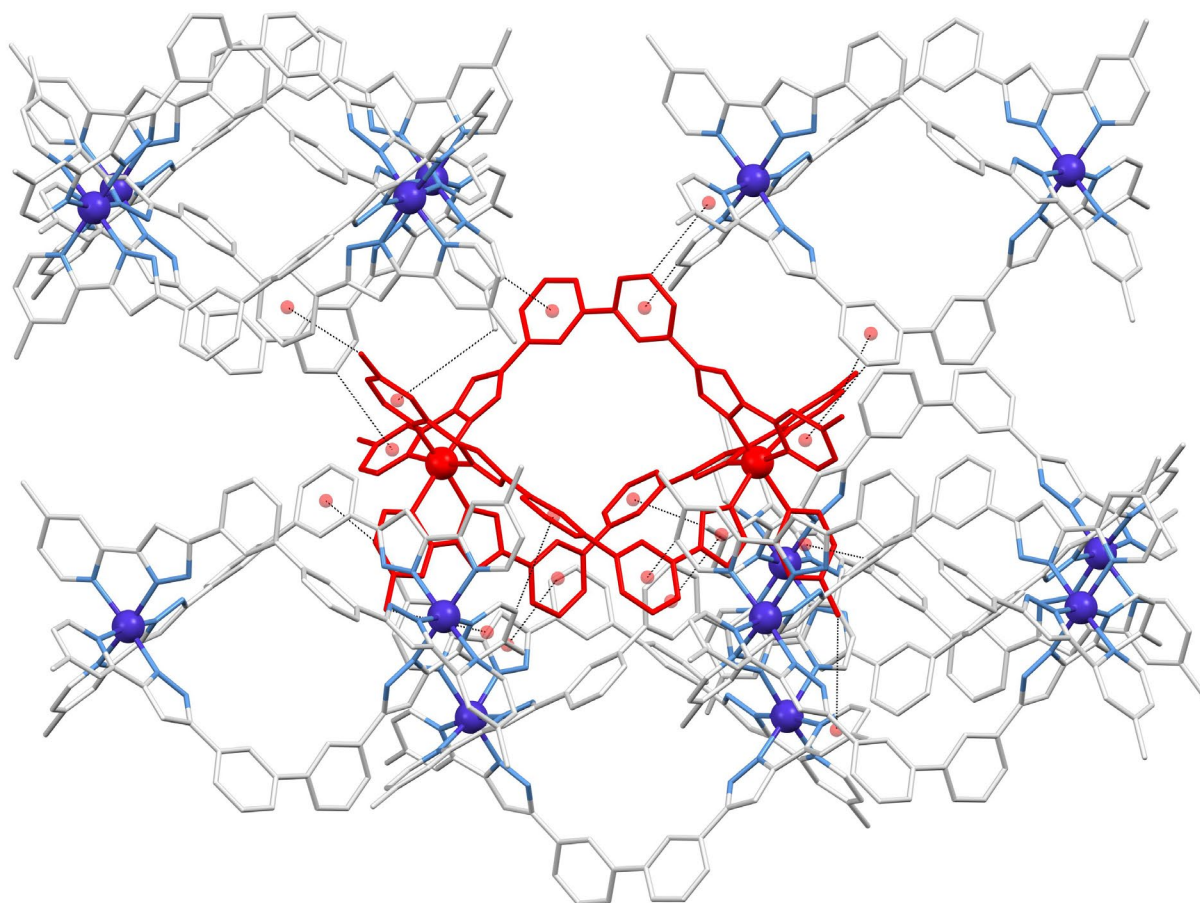


Figure S5. Representation of one $(\text{ClO}_4@[\text{Co}_2(\text{L}2)_3])^{3+}$ unit from **3** (red) together with its seven first neighbors in the crystal lattice (the latter with dark blue, light blue and grey representing Co, N and C respectively). The interactions with these neighbors are $\pi \cdots \pi$ or $\text{C-H} \cdots \pi$ interactions emphasized by contacts between the centroids (red balls linked by dashed black lines) of the aromatic rings involved or between centroids and the carbon atom of the C-H group involved (also linked by dashed black lines). H atoms not shown for clarity.

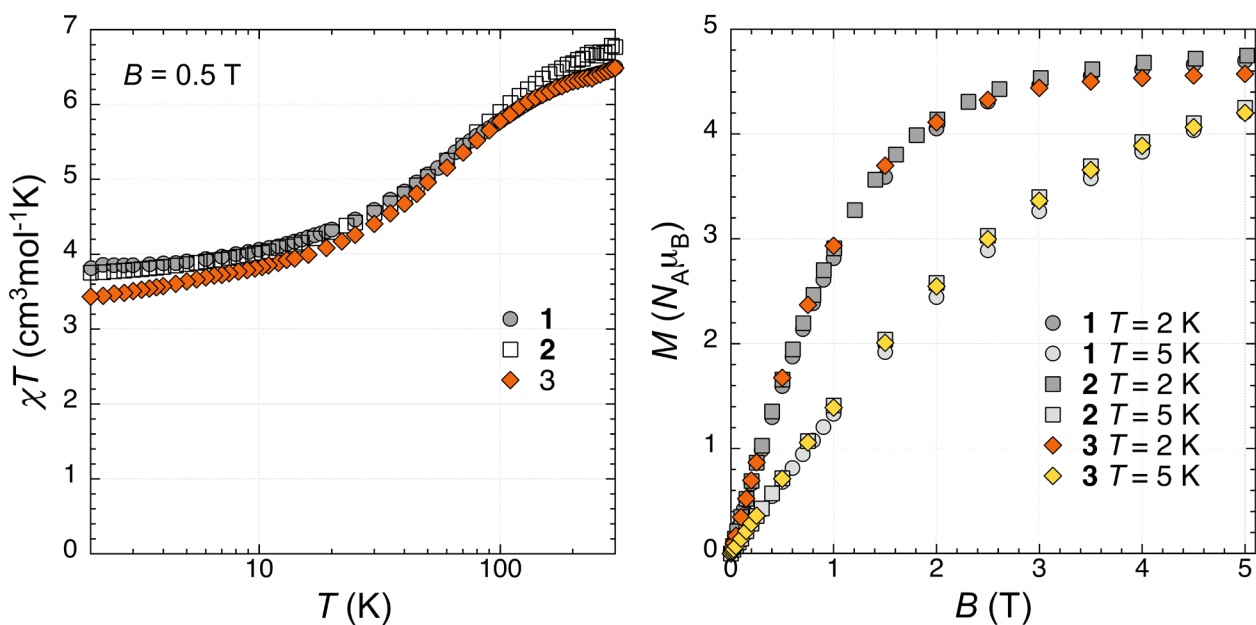


Figure S6. Left: temperature dependence of χT for compounds **1**, **2** and **3**, as indicated. Right: magnetization isotherms at 2 and 5 K for compounds **1**, **2** and **3**, as indicated.

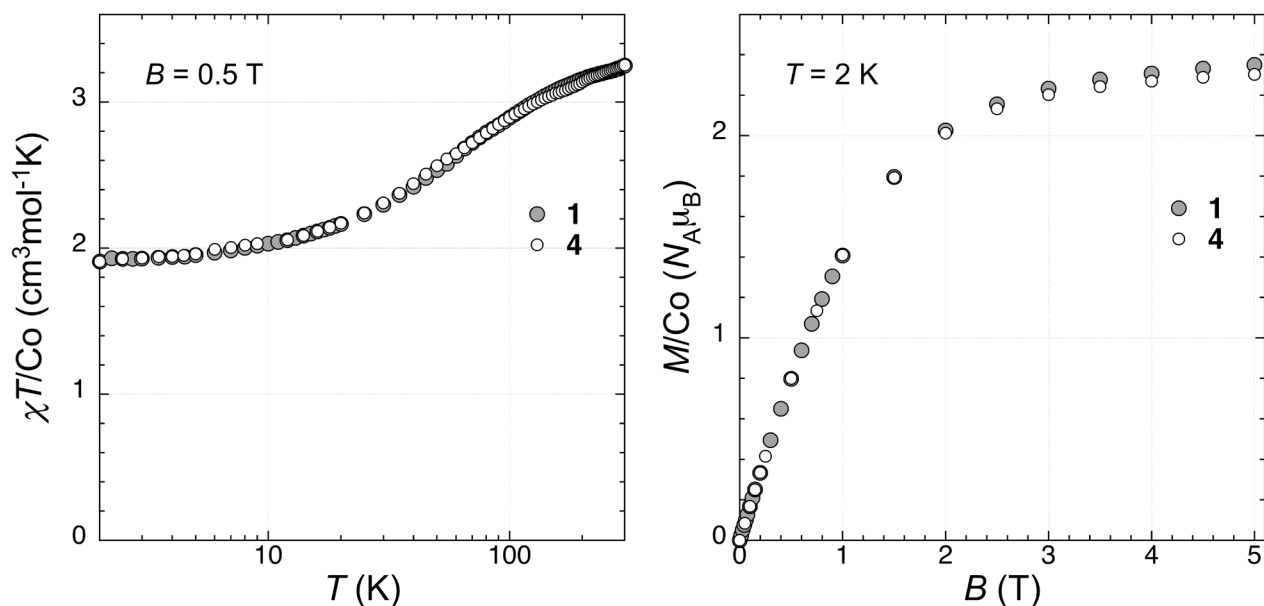


Figure S7. Left: temperature dependence of χT for compounds **1**, and **4** normalized per Co(II) ion, as indicated. Right: magnetization isotherms at 2 K for compounds **1**, and **4** normalized per Co(II) ion, as indicated.

CASSCF-SO calculations

Due to the large separation between Co(II) ions, we assume that the measured magnetic properties in **1-3** arise from the independent contribution of each ion. Thus, for each compound we define two analogues (**X^a** and **X^b**) where one of the Co(II) ions has been substituted by its structurally analogous diamagnetic Zn(II) ion.

A possible magnetic interaction between the Co(II) centres in each compound is calculated as

$$\bar{J}_{ab}^{dip} = -\frac{\mu_B^2 \mu_0}{4\pi} \frac{1}{\|\vec{R}_{ba}\|^3} [\bar{g}_a \bar{g}_b - 3(\bar{g}_a \vec{R}_{ba})(\vec{R}_{ba}^T \bar{g}_b)]$$

Where the minus sign comes from a $\hat{H} = -\hat{S}_a \bar{J}_{ab}^{dip} \hat{S}_b$ formalism, so $J^{dip} = \Delta E$. One should use a conversion factor of 5.034E+22 between Joules and cm⁻¹. In what follows, the g-tensors are calculated at different levels of theory.

The electronic structure and g-tensors of compounds **1^{a,b}**-**3^{a,b}** have been investigated at the complete active space self-consistent field (CASSCF) level using OpenMolcas.v21.⁹ Scalar relativistic effects were taken into account through the ANO-RCC basis set library,^{10,11} in combination with a second-order Douglas–Kroll–Hess Hamiltonian transformation – depending on the atom, the quality of the basis set varied: VQZP for the Co atoms, VTZP for Co-coordinating atoms, VDZP for Zn and counterion guest atoms and VDZ for the remaining atoms. Cholesky decomposition of the two-electron integrals with a threshold of 10⁻⁸ was performed to save disk space and reduce computational demand. The molecular orbitals (MOs) were optimized in a state averaged CASSCF calculations within each spin manifold defined by 7 electrons in the 5 3d orbitals: 10 roots for the spin quartet (⁴F, ⁴P) and 40 roots for the spin doublet (²G, ²P, ²H, ²D, ²D, ²F). Then, using the restricted-active-space state-interaction spin-orbit (RASSI-SO) formalism,^{12,13} these spin-free wavefunctions (10 quartet and 40 doublet states) were mixed, with spin-orbit coupling matrix elements calculated by the atomic-mean-field approximation¹² to the Breit–Pauli Hamiltonian. Finally, working with these CASSCF-RASSI-SO wavefunctions, simulations of magnetisation and susceptibility curves were obtained using the SINGLE_ANISO module.¹⁴ The results following this procedure are presented in Tables S4-S6.

Knowing that *i*) the first three free ion terms of a d⁷ electronic configuration are ⁴F, ⁴P and ²G and that *ii*) in an octahedral ligand field these split into ⁴A_{2g} + ⁴T_{1g} + ⁴T_{2g}, ⁴T_{1g} and ²A_{1g} + ²E_g + ²T_{1g} + ²T_{2g}, respectively,¹⁵ the calculated pattern of the spin-free states (Tables S4-S6) can be tentatively classified as follows: from the ⁴F, the ⁴T_{1g} + ⁴T_{2g} states make up the lowest six roots, which are well isolated from the ⁴A_{2g} (ca. 17000 cm⁻¹); the ⁴T_{1g} states from the ⁴P term appear much higher in energy (ca. 25000 cm⁻¹). Finally, the doublet ²E_g and triplets ²T_{1g} + ²T_{2g} terms from the parent ²G make up for states 7-8 and 10-15, respectively. Focusing now on the spin-orbit coupled states, we see the pairing of states forming Kramers doublets (KD). The first 12 KDs span ca 9000 cm⁻¹ and are well isolated from the 13th KD (ca. 14000 cm⁻¹) – inspection of their wavefunction composition reveals

⁹ G. L. Manni *et al*, *J. Chem. Theory Comput.* **2023**, 19, 20, 6933–6991

¹⁰ B. O. Roos, R. Lindh, P.-Å. Malmqvist, V. Veryazov and P.-O. Widmark, *J. Phys. Chem. A.* **2004**, 108, 2851–2858

¹¹ B. O. Roos, R. Lindh, P.-Å. Malmqvist, V. Veryazov and P.-O. Widmark, *J. Phys. Chem. A.* **2005**, 109, 6575–6579

¹² H. Bernd *et al*, *Chem. Phys. Lett.* **1996**, 251, 365–371

¹³ P. Å., Malmqvist, *Chem. Phys. Lett.* **2002**, 357, 230–240

¹⁴ L. Ungur and L. F. Chibotaru, *Chem. Eur. J.* **2017**, 23, 3708–3718

¹⁵ F. Lloret *et al.*, *Inorg. Chim. Acta* **2008**, 361, 3432–3445

that first 12 KDs are almost 100% composed by the first six spin-only states, i.e., linear combinations of the $^4T_{1g} + ^4T_{2g}$ states coming from the 4F free ion term. This pattern is maintained for all **1-3** compounds and follows what has been observed for other Co(II) complexes, where the magnetic properties are dominated by the $^4T_{1g}$ states.¹⁵

Compound **1** presents a large variation of the g-tensors and energy splitting of the low-lying states when comparing the two coordination pockets (Table S4), which translates into a noticeable difference in the magnetic susceptibility. This is likely due to the different distances between coordinating ligands in each pocket. Compounds **2** and **3** do not present such marked differences and their susceptibilities and magnetisation curves are virtually superimposable. Finally, the calculated dipolar coupling vectors are presented in Table S10-S12; considering only the main component, **1** presents a value twice as big as that for **3**. This is in contrast with estimates from heat capacity measurements, that point to an averaged dipolar field $\langle B_{\text{dip}} \rangle$ of c.a. 6, 24 and 28 mT respectively for **1**, **2** and **3**.

Applying the same CASSCF-RASSI-SO procedure outlined above but with a larger basis set (VQZP for the Co atoms, VTZP for Co-coordinating atoms, VDZP for the remaining atoms) for **1a** did not change the results (Table S7).

Applying the same CASSCF-RASSI-SO procedure outlined above but with a larger active space consisting of 7 electrons in 10 orbitals (both 3- and 4-*d* orbitals) for **1a** did not change the results either (Table S8).

Table S4. Energies (cm^{-1}) of spin-only and spin-orbit coupled states of **1** calculated at the CAS(7,5)SCF-SO-RASSI with 10 quartets and 40 doublets level, using the crystal structure. For spin-only states, lighter and darker grey indicate quartet and doublets spin multiplicities, respectively. For spin-orbit coupled states, each row is a Kramers doublet, where the g-values of the first 12 doublets are also shown.

1^a					1^b				
Spin-only		Spin-orbit			Spin-only		Spin-orbit		
E (cm^{-1})	E (cm^{-1})	g_x	g_y	g_z	E (cm^{-1})	E (cm^{-1})	g_x	g_y	g_z
0.00	0.00	2.833	4.526	5.617	0.00	0.00	2.028	3.250	6.976
341.90	223.75	0.452	0.517	5.329	582.22	150.51	1.615	1.726	5.616
539.48	534.84	2.144	2.826	3.862	1254.59	754.45	1.212	3.039	5.302
7815.37	928.34	0.134	0.423	3.450	7397.33	1017.95	0.809	0.875	3.749
7930.15	1070.72	0.634	2.060	2.685	7807.70	1563.22	1.019	1.834	5.130
8244.53	1185.60	0.229	0.291	3.456	7990.47	1667.05	1.294	1.408	4.148
13349.80	8172.20	1.310	1.610	5.715	14370.36	7653.32	0.057	0.086	6.458
13834.87	8207.54	1.601	2.493	4.869	14836.35	7705.95	2.143	3.764	3.919
16977.32	8317.04	1.283	2.911	4.456	15973.19	8070.07	1.593	2.871	4.976
19924.64	8385.66	0.782	0.916	4.527	20129.49	8119.24	0.894	1.240	4.892
20148.53	8637.71	0.046	0.080	6.273	20479.89	8275.78	0.424	0.483	6.060
20173.81	8745.13	2.180	3.286	3.368	20568.06	8387.00	2.145	2.855	3.614
20253.64	13752.08	-			20725.11	14651.13	-		
20585.48	[...]				20887.65	[...]			
20706.20	74217.87				21184.87	74068.60			
24483.18					24404.27				
24799.30					24518.93				
25083.24					25026.24				
25977.91	-				25808.15	-			
[...]					[...]				
73594.48					73599.23				

Table S5. Energies (cm^{-1}) of spin-only and spin-orbit coupled states of **2** calculated at the CAS(7,5)SCF-SO-RASSI with 10 quartets and 40 doublets level, using the crystal structure. For spin-only states, lighter and darker grey indicate quartet and doublets spin multiplicities, respectively. For spin-orbit coupled states, each row is a Kramers doublet, where the g-values of the first 12 doublets are also shown.

2^a					2^b				
Spin-only		Spin-orbit			Spin-only		Spin-orbit		
E (cm^{-1})	E (cm^{-1})	g_x	g_y	g_z	E (cm^{-1})	E (cm^{-1})	g_x	g_y	g_z
0.00	0.00	2.738	3.657	6.456	0.00	0.00	3.029	3.334	6.551
260.61	232.01	0.846	1.412	4.937	82.99	262.90	0.254	1.839	3.470
609.64	519.52	1.477	2.822	3.456	512.64	460.30	0.836	1.258	2.047
7746.85	902.17	0.211	0.383	3.397	7351.69	873.65	0.291	0.482	3.290
7758.01	1123.54	0.799	1.743	3.850	7501.06	1101.17	0.633	1.079	4.419
7927.69	1228.39	0.844	0.947	3.589	7588.77	1203.44	1.323	1.564	3.367
13638.84	8075.74	1.517	2.467	5.385	13850.12	7793.21	0.671	1.072	6.051
13773.61	8125.58	0.432	2.180	3.867	13968.24	7837.19	1.840	3.066	4.545
16568.03	8167.43	0.461	1.487	3.130	15988.17	7954.80	1.292	2.230	5.233
19943.23	8241.21	0.722	0.961	3.923	19927.39	8013.36	1.042	1.414	4.287
20054.90	8350.24	0.071	0.098	5.893	19986.59	8090.88	0.047	0.072	5.720
20235.57	8484.38	2.340	2.927	3.296	20200.39	8232.73	2.394	2.758	3.353
20352.21	14052.74	-			20270.30	14336.92	-		
20391.85	[...]				20326.78	[...]			
20569.47	74015.97				20504.30	73747.18			
24271.04					24072.84				
24698.22					24434.90				
24849.87					24488.91				
25867.54					25560.42				
[...]					[...]				
73385.96	-				73007.17	-			

Table S6. Energies (cm^{-1}) of spin-only and spin-orbit coupled states of **3** calculated at the CAS(7,5)SCF-SO-RASSI with 10 quartets and 40 doublets level, using the crystal structure. For spin-only states, lighter and darker grey indicate quartet and doublets spin multiplicities, respectively. For spin-orbit coupled states, each row is a Kramers doublet, where the g-values of the first 12 doublets are also shown.

3^a					3^b				
Spin-only		Spin-orbit			Spin-only		Spin-orbit		
E (cm^{-1})	E (cm^{-1})	g_x	g_y	g_z	E (cm^{-1})	E (cm^{-1})	g_x	g_y	g_z
0.00	0.00	2.852	4.980	5.202	0.00	0.00	2.723	4.356	5.858
384.14	228.79	0.009	0.181	5.343	348.77	222.92	0.488	0.824	5.237
446.23	536.12	2.590	2.823	3.663	562.39	546.07	1.897	2.900	4.022
7727.07	960.21	0.308	0.617	2.694	8059.82	940.56	0.035	0.538	3.168
8192.80	1022.84	0.302	0.775	1.946	8177.91	1078.87	0.462	0.806	3.837
8240.68	1146.19	0.529	0.538	3.289	8268.96	1195.37	1.190	1.345	3.294
13134.45	8108.82	0.216	0.261	6.345	13307.07	8406.46	1.258	2.406	5.340
13848.50	8159.99	2.090	3.651	4.058	13600.11	8443.06	1.287	1.839	5.206
17090.26	8529.50	1.867	2.450	5.461	17296.09	8526.51	0.982	1.766	5.443
19885.17	8590.38	0.218	1.613	3.817	19921.79	8595.08	1.094	1.904	3.488
20088.16	8661.66	0.219	0.436	4.776	20161.11	8677.27	0.060	0.259	5.527
20126.78	8804.75	2.156	2.336	3.734	20257.82	8822.42	2.370	2.749	3.373
20272.30	13546.26	-			20375.66	13705.99	-		
20397.60	[...]				20499.69	[...]			
20862.92	74500.84				20694.78	74566.37			
24413.25					24651.69				
24720.94					24823.42				
25432.10					25387.38				
25929.36					26006.06				
[...]					[...]				
73915.06	-				73969.47	-			

Table S7. Energies (cm^{-1}) of spin-only and spin-orbit coupled states of 1^a calculated at the CAS(7,5)SCF-SO-RASSI, with 10 quartets and 40 doublets and larger basis set level, using the crystal structure. For spin-only states, lighter and darker grey indicate quartet and doublets spin multiplicities, respectively. For spin-orbit coupled states, each row is a Kramers doublet, where the g-values of the first 12 doublets are also shown. Percentage errors relative to the CAS(7,5)SCF-SO-RASSI results (Table S4) are also shown

1^a									
Spin-only		Spin-orbit							
E (cm^{-1})	% <i>err</i>	E (cm^{-1})	% <i>err</i>	g_x	% <i>err</i>	g_y	% <i>err</i>	g_z	% <i>err</i>
0.00	0	0.00	0	2.825	0	4.495	-1	5.650	1
339.63	-1	223.20	0	0.470	4	0.554	7	5.325	0
548.00	2	535.41	0	2.099	-2	2.838	0	3.876	0
7788.27	0	926.55	0	0.167	20	0.423	0	3.460	0
7909.01	0	1075.71	0	0.642	1	1.983	-4	2.842	6
8221.28	0	1190.17	0	0.327	30	0.384	24	3.464	0
13373.72	0	8145.39	0	1.200	-9	1.456	-11	5.805	2
13855.69	0	8180.75	0	1.670	4	2.643	6	4.790	-2
16925.05	0	8295.26	0	1.302	1	2.939	1	4.475	0
19923.38	0	8362.36	0	0.774	-1	0.916	0	4.549	0
20146.09	0	8614.17	0	0.041	-13	0.075	-7	6.264	0
20174.35	0	8721.09	0	2.178	0	3.293	0	3.363	0
20258.44	0	13775.09		-					
20580.95	0	[...]		-					
20701.47	0	74192.09		-					
24457.26	0			-					
24784.53	0			-					
25059.89	0			-					
25970.85	0			-					
[...]				-					
73568.94	0			-					

Table S8. Energies (cm^{-1}) of spin-only and spin-orbit coupled states of 1^a calculated at the CAS(7,10)SCF-SO-RASSI with 10 quartets and 40 doublets level using the crystal structure. For spin-only states, lighter and darker grey indicate quartet and doublets spin multiplicities, respectively. For spin-orbit coupled states, each row is a Kramers doublet, where the g-values of the first 12 doublets are also shown. Percentage errors relative to the CAS(7,5)SCF-SO-RASSI results (Table S4) are also shown.

1^a									
Spin-only		Spin-orbit							
E (cm^{-1})	% ^{err}	E (cm^{-1})	% ^{err}	g_x	% ^{err}	g_y	% ^{err}	g_z	% ^{err}
0.00	0	0.00	0	2.746	-3	4.452	-2	5.665	1
353.65	3	207.32	-8	0.519	13	0.565	8	5.362	1
561.73	4	531.41	-1	2.056	-4	2.858	1	4.011	4
8498.77	8	894.98	-4	0.188	29	0.478	12	3.472	1
8615.36	8	1047.65	-2	0.660	4	2.141	4	2.746	2
8945.77	8	1160.95	-2	0.227	-1	0.276	-5	3.528	2
12221.95	-9	8824.38	7	1.550	15	1.986	19	5.544	-3
12732.21	-9	8852.35	7	1.452	-10	2.122	-17	5.119	5
18320.89	7	8967.67	7	1.299	1	2.799	-4	4.587	3
19440.99	-2	9032.67	7	0.920	15	1.052	13	4.566	1
19656.55	-3	9302.21	7	0.039	-18	0.065	-23	6.266	0
19748.43	-2	9401.98	7	2.168	-1	3.351	2	3.417	1
19921.00	-2	12601.18		-					
20336.21	-1	[...]							
20479.07	-1	72039.44							
23863.33	-3								
24166.09	-3								
24477.17	-2								
25506.36	-2								
[...]									
71391.78	-3								

Table S9. \vec{j}^{dip} (cm⁻¹) components calculated between the *g*-tensors of the ground Kramers for **1^a** and **1^b** respectively, at the CAS(5,7)SCF-SO-RASSI level of theory (Table 4). parameters.

\bar{g}_a			\bar{g}_b			\vec{j}_{ab}^{dip}
3.434	-0.767	0.384	4.971	-1.517	-1.886	-0.0019
-0.767	4.820	0.796	-1.517	3.379	0.356	-0.0067
0.384	0.796	4.722	-1.886	0.356	3.903	-0.016

Table S10. \vec{j}^{dip} (cm⁻¹) components calculated between the *g*-tensors of the ground Kramers doublet for **2^a** and **2^b** respectively, at the CAS(5,7)SCF-SO-RASSI level of theory (Table 5). parameters.

\bar{g}_a			\bar{g}_b			\vec{j}_{ab}^{dip}
4.896	-1.340	-0.919	5.393	1.4047	-0.671	-0.0034
-1.340	4.799	0.391	1.405	4.101	-0.617	-0.0075
-0.919	0.391	3.156	-0.671	-0.617	3.420	-0.012

Table S11. \vec{j}^{dip} (cm⁻¹) components calculated between the *g*-tensors of the ground Kramers doublet for **3^a** and **3^b** respectively, at the CAS(5,7)SCF-SO-RASSI level of theory. Parameters (Table 6).

\bar{g}_a			\bar{g}_b			\vec{j}_{ab}^{dip}
2.942	-0.352	-0.281	3.063	0.258	-0.900	-0.0022
-0.352	5.121	0.028	0.258	4.768	-0.619	-0.0066
-0.281	0.028	4.970	-0.900	-0.620	5.106	-0.0085

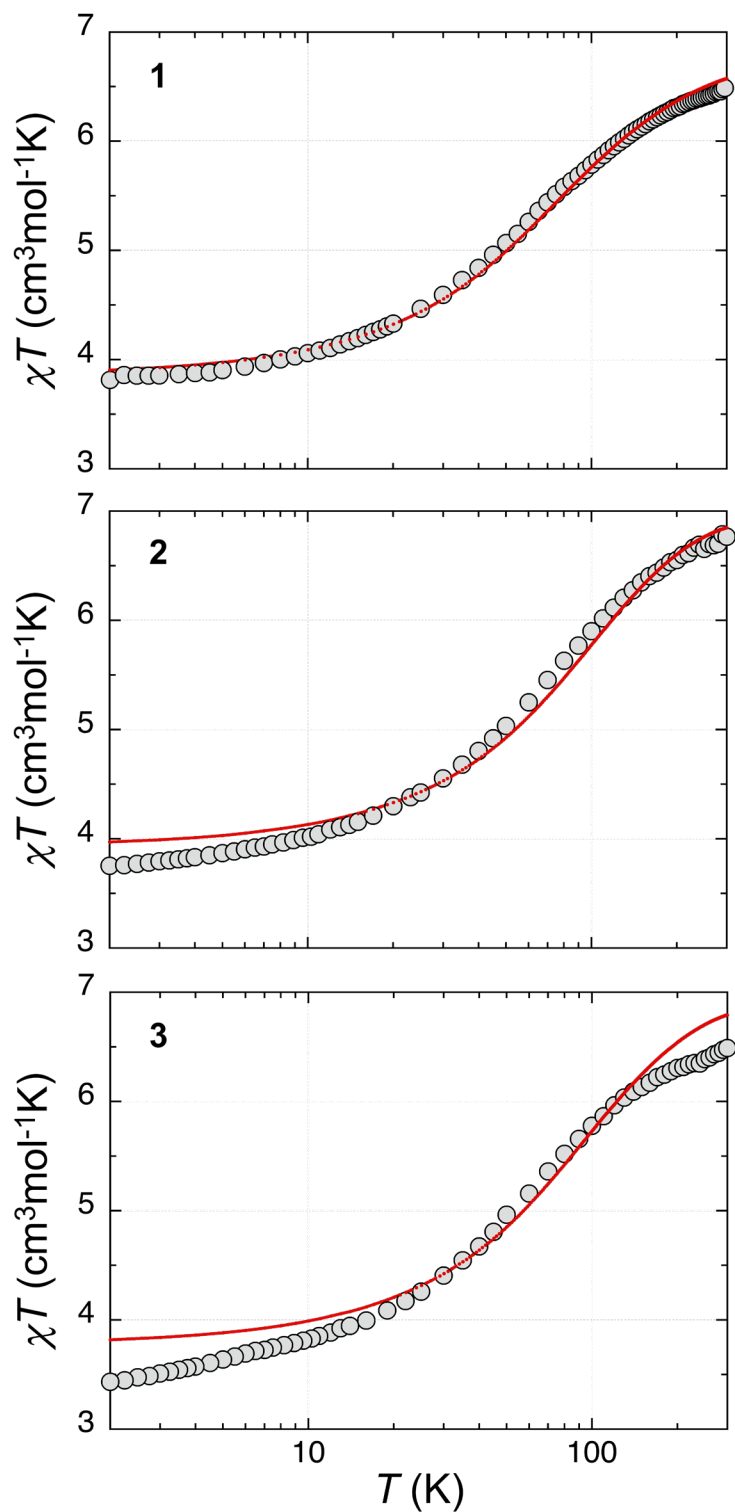


Figure S8. Semi-log χT vs. T comparative plot of experimental (grey dots) and CASSCF-RASSI-SO calculated (red solid lines) for compounds **1**, **2** and **3**. Data were acquired under 200 (2-20 K) and 3000 (2-300 K) Oe dc field, and compared satisfactorily with data derived from zero-field ac susceptibility in the 2-10 K range give similar values of χ , ensuring these represent the equilibrium susceptibility.

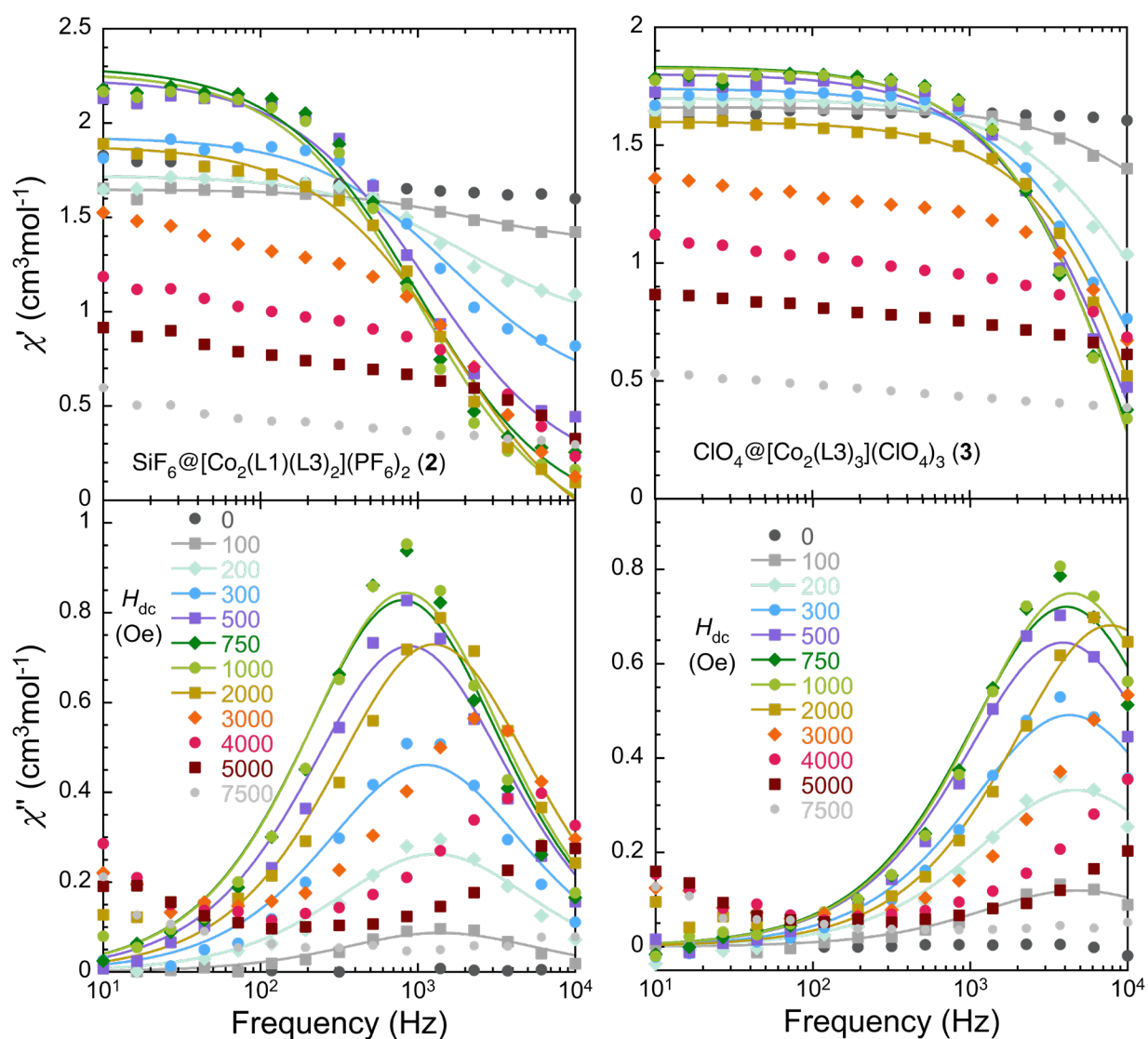


Figure S9. Frequency dependence of the in-phase (top) and out-of-phase (bottom) ac magnetic susceptibility of compounds **2** (left) and **3** (right) at 2 K and increasing applied dc fields as indicated. Lines are fits of the experimental data to the Cole-Cole expressions for the real and imaginary susceptibility.

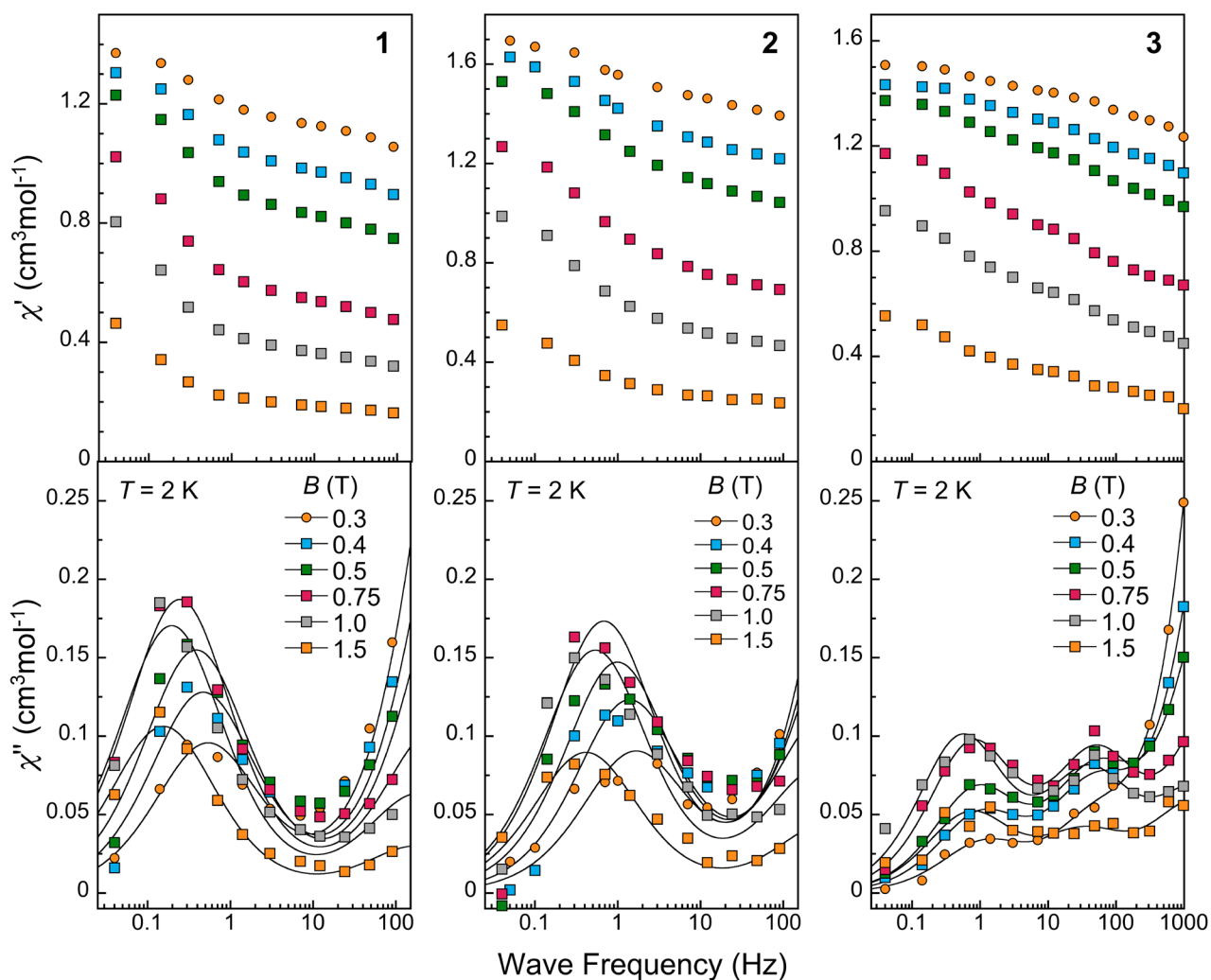


Figure S10. Low frequency dependence of the in-phase (top) and out-of-phase (bottom) ac magnetic susceptibility of compounds **1** (left) and **2** (middle) and **3** (right) at 2 K and increasing fields as indicated. Lines are fits of the experimental data to a bimodal model in the case of **1** and **2**, and trimodal model in the case of **3**.

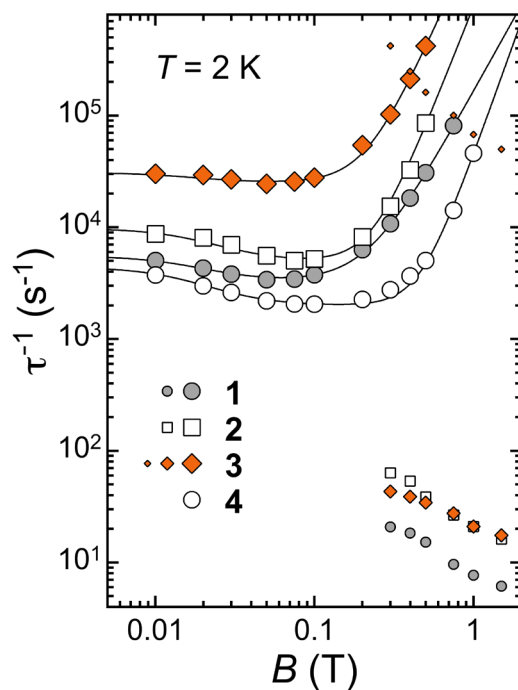


Figure S11. Field dependence of the magnetization relaxation rates of compounds **1-4**, as indicated. Smaller symbols correspond to a second (and third in the case of **3**) slower relaxation mode that becomes dominant at the highest fields. Full lines are fits of the faster component to the expressions $\tau^{-1} = CB^n + D(1+EB^2)/(1+FB^2)$ (see text and Table S13).

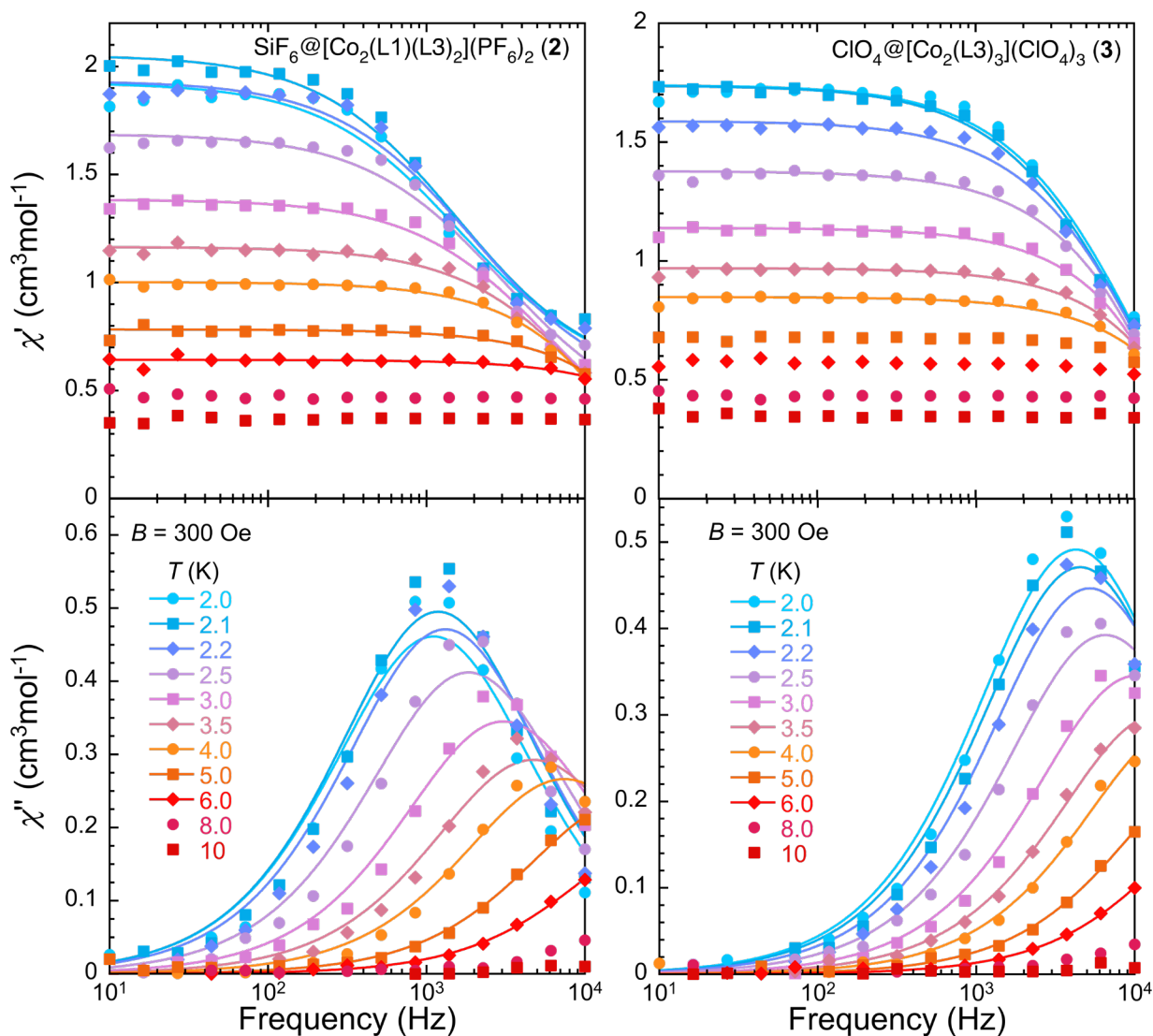


Figure S12. Frequency dependence of the in-phase (top) and out-of-phase (bottom) ac magnetic susceptibility of compounds **2** (left) and **3** (right) at 0.03 T and increasing temperatures as indicated. Lines are fits of the experimental data to the Cole-Cole expressions for the real and imaginary susceptibility.

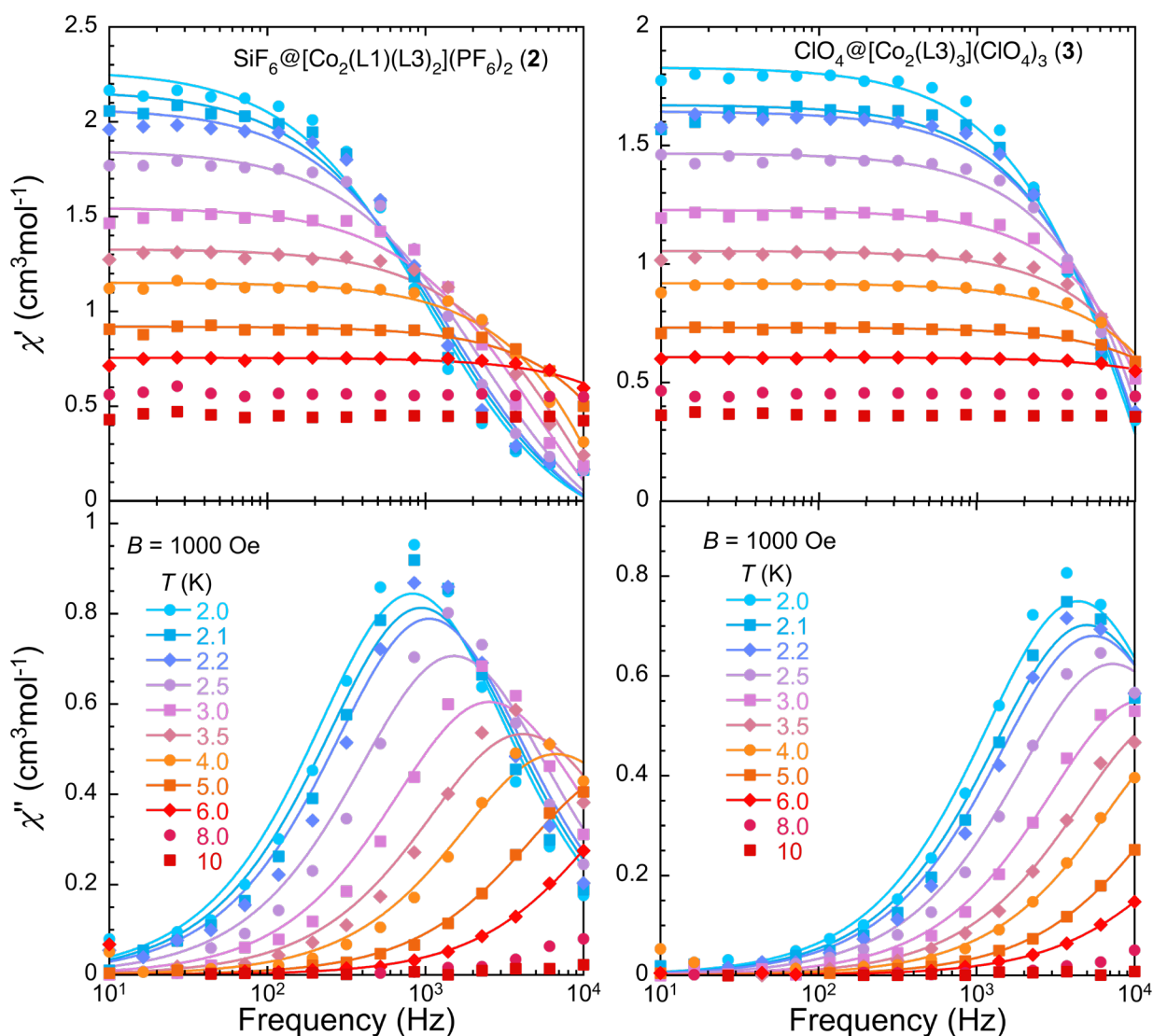


Figure S13. Frequency dependence of the in-phase (top) and out-of-phase (bottom) ac magnetic susceptibility of compounds **2** (left) and **3** (right) at 0.1 T and increasing temperatures as indicated. Lines are fits of the experimental data to the Cole-Cole expressions for the real and imaginary susceptibility.

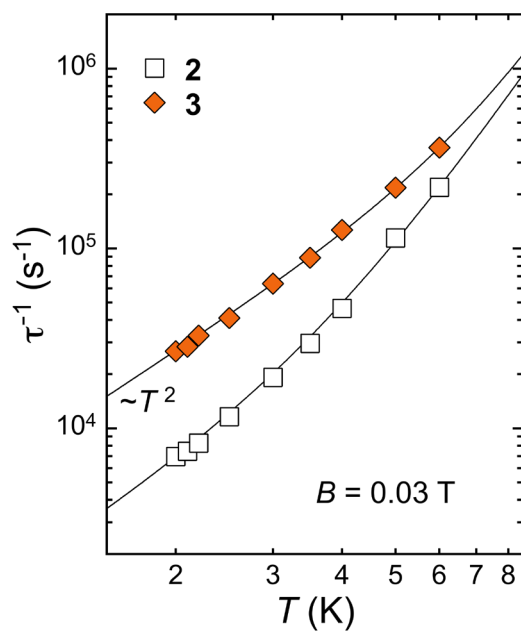


Figure S14. Temperature dependence of the magnetization relaxation rates of compounds 2 and 3 under a 0.03 T applied field. Full lines are a fit to $\tau^{-1} = AT^2 + BT^m$ (see Table S14).

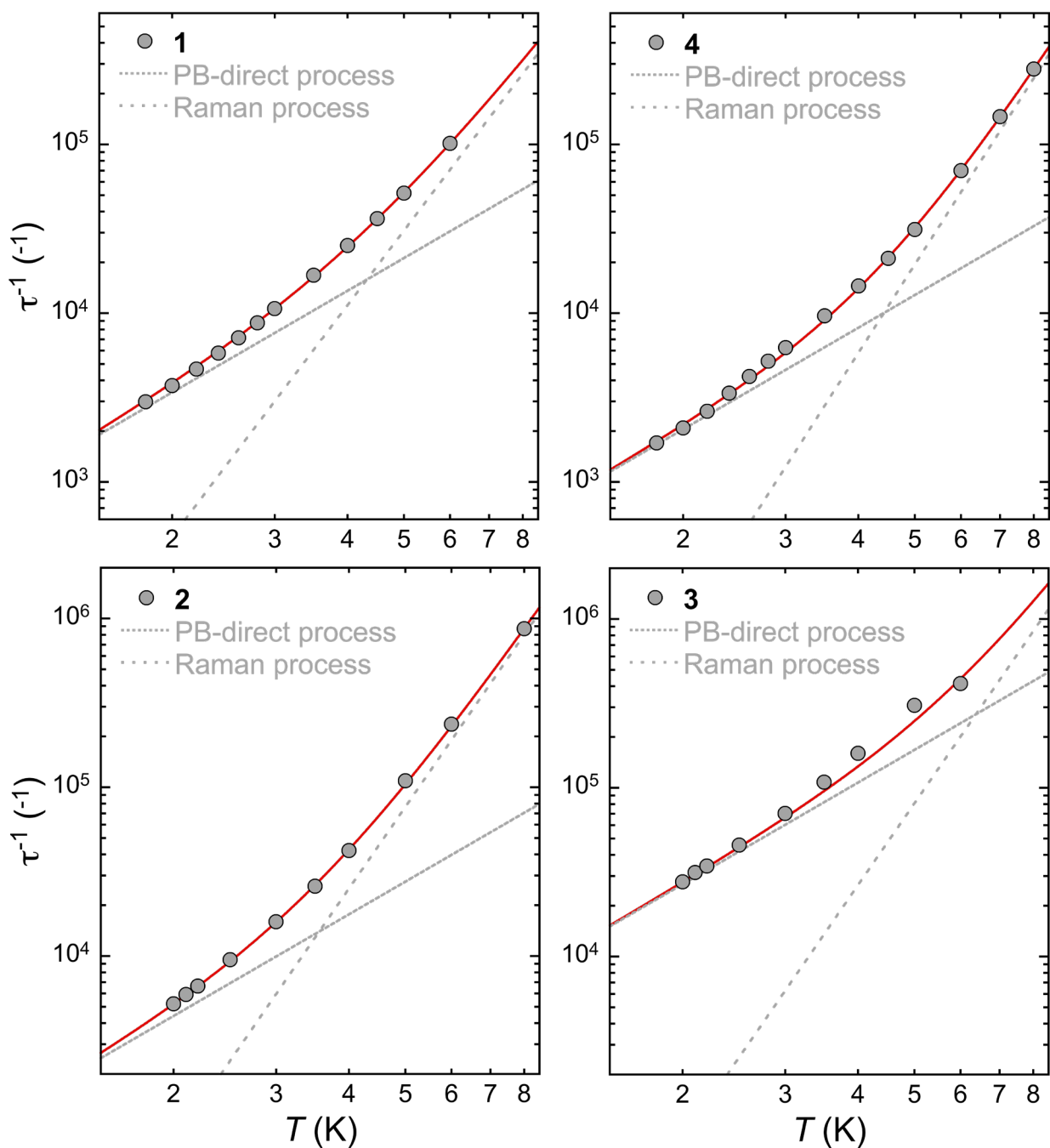


Figure S15. Temperature dependence of the magnetization relaxation rates of compounds **1**, **2**, **3** and **4** under a 0.1 T applied field, as indicated, showing the two components of the simulation (red lines) using the expression $\tau^{-1} = AT^2 + BT^m$ (see Table S14): the phonon-bottlenecked direct process (dotted grey lines) and the Raman process (dashed grey lines).

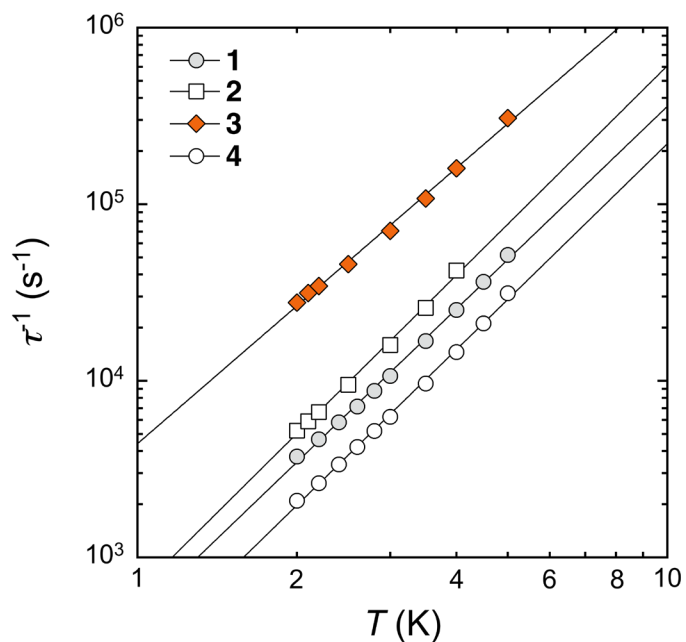


Figure S16. Temperature dependence of the magnetization relaxation rates of compounds **1-4** under a 0.1 T applied field in the range for which the data can be reproduced with a single power law $\sim T^n$, with $n = 2.88, 2.98, 2.59$ and 2.93 respectively (full lines).

Table S12. Parameters that provide the best fit to the field dependence of the relaxation rate τ^{-1} for compounds **1-4**.

$$\tau^{-1} = CB^n + D \left(\frac{1 + EB^2}{1 + FB^2} \right)$$

	C (T ⁻ⁿ s ⁻¹)	n	D (s ⁻¹)	E (T ⁻²)	F (T ⁻²)
1	1.62(2)x10 ⁵	2.57(3)	5.5(4)x10 ³	1877(160)	3200
2	9.41(3)x10 ⁵	3.6(1)	9.8(2)x10 ³	1200	2400
3	36(2)x10 ⁵	3.1(1)	31(2)x10 ³	2900	3600
4	4.35(6)x10 ⁴	4	4.4(4)x10 ³	1490	3300

Table S13. Parameters that provide the best fit to the temperature dependence of the relaxation rate τ^{-1} for compounds **1-4**.

$$\tau^{-1} = AT^2 + BT^m$$

	B (T)	A ($\text{K}^{-2} \text{s}^{-1}$)	B ($\text{K}^{-m} \text{s}^{-1}$)	m
1	0.1	849(33)	20(4)	4.6(1)
2	0.1	1103(30)	24.5(1)	5
	0.03	1453(20)	49(11)	4.5(2)
3	0.1	6700(50)	26(3)	5
	0.03	6635(50)	16.1(3)	5
4	0.1	513(25)	3.2(4)	5.4(1)

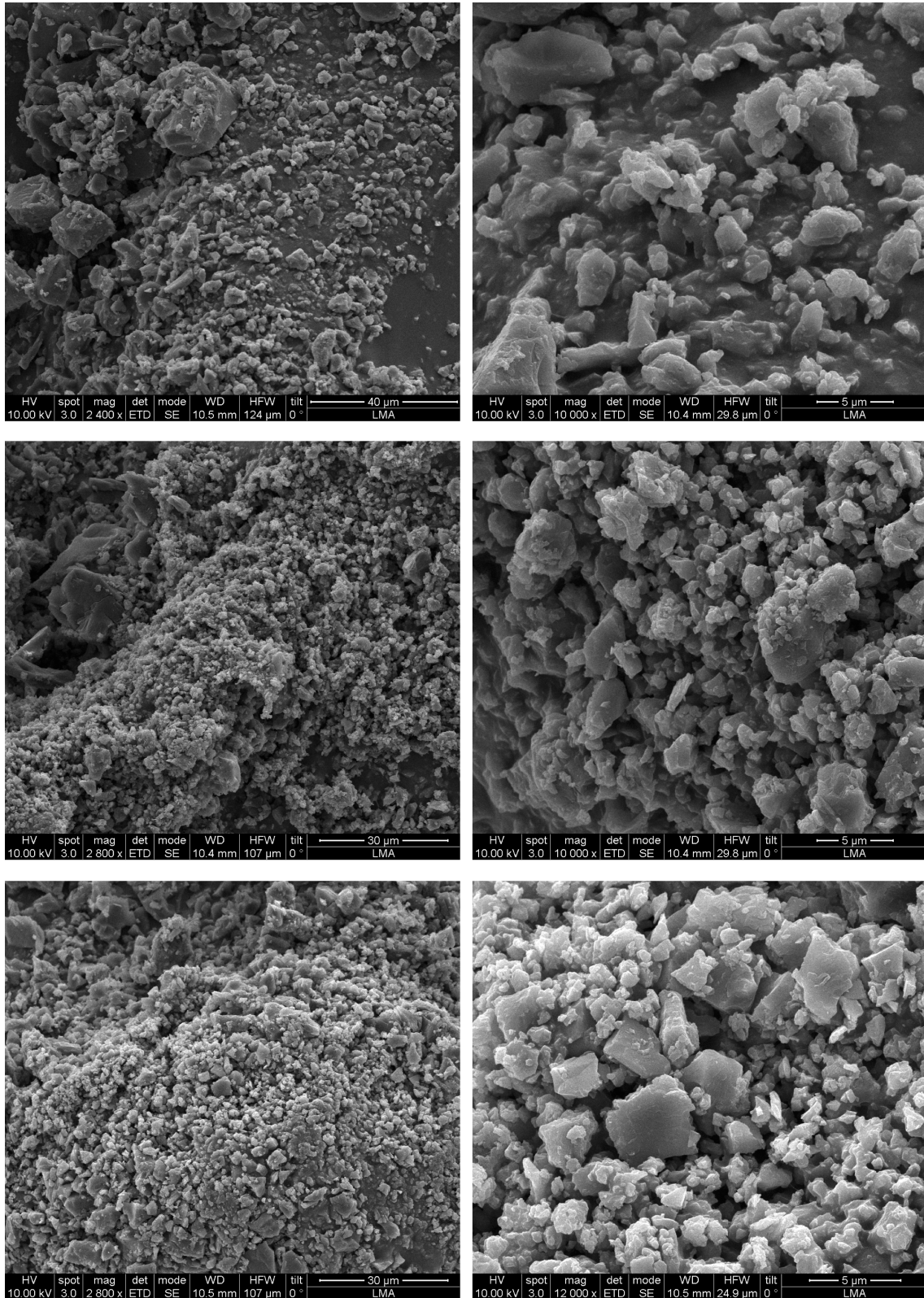


Figure S17. Representative SEM images of the polycrystalline samples used in the magnetic study at two different magnifications: **1**, top; **2**, middle; **3**, bottom. Analysis over various images confirmed the absence of significantly larger crystals, the crystallites being relatively homogeneous, with representative largest dimensions in the 0.5-25, 0.5-10 and 0.5-10 μm ranges, respectively for **1**, **2** and **3**.

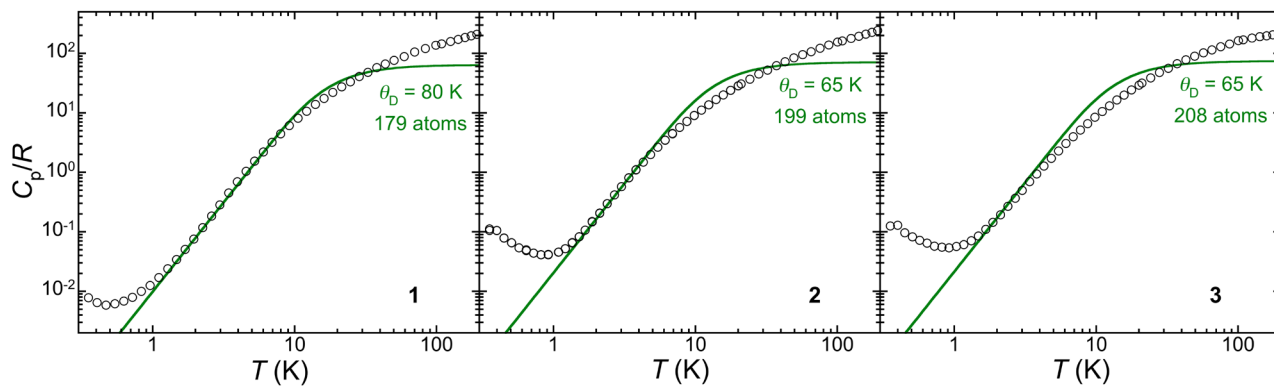


Figure S18. Specific heat of **1,2** and **3** in zero applied field, as indicated. The full green lines are the calculated Debye heat capacity for the adequate number of atoms and Debye temperature θ_D that best reproduces the lower temperature lattice heat capacity. Note how these calculated Debye heat capacity significantly surpass the experimental ones.